

SpikeReveal: Unlocking Temporal Sequences from Real Blurry Inputs with Spike Streams

Kang Chen^{1*†}, Shiyao Chen^{2*}, Jiyuan Zhang^{2*}, Baoyue Zhang³
Yajing Zheng^{2✉}, Tiejun Huang², and Zhaofei Yu^{2✉}

¹ WuHan University

kangchen0623@gmail.com

² School of Computer Science, Peking University

{strerichia002p, jy Zhang}@stu.pku.edu.cn

{y.j.zheng, yuzf12, tj Huang}@pku.edu.cn

³ Dalian University of Technology

yanyao_715@163.com

Abstract. Reconstructing a sequence of sharp images from the blurry input is crucial for enhancing our insights into the captured scene and poses a significant challenge due to the limited temporal features embedded in the image. Spike cameras, sampling at rates up to 40,000 Hz, have proven effective in capturing motion features and beneficial for solving this ill-posed problem. Nonetheless, existing methods fall into the supervised learning paradigm, which suffers from notable performance degradation when applied to real-world scenarios that diverge from the synthetic training data domain. Moreover, the quality of reconstructed images is capped by the generated images based on motion analysis interpolation, which inherently differs from the actual scene, affecting the generalization ability of these methods in real high-speed scenarios. To address these challenges, we propose the first self-supervised framework for the task of spike-guided motion deblurring. Our approach begins with the formulation of a spike-guided deblurring model that explores the theoretical relationships among spike streams, blurry images, and their corresponding sharp sequences. We subsequently develop a self-supervised cascaded framework to alleviate the issues of spike noise and spatial-resolution mismatching encountered in the deblurring model. With knowledge distillation and re-blurring loss, we further design a lightweight deblur network to generate high-quality sequences with brightness and texture consistency with the original input. Quantitative and qualitative experiments conducted on our real-world and synthetic datasets with spikes validate the superior generalization of the proposed framework. Our code, data and trained models will be available at <https://github.com/chenkang455/S-SDM>.

Keywords: Motion Deblur · Spike Camera · Self-supervised

* Equal contributors.

✉ Corresponding authors.

† Work done during an internship at Peking University.

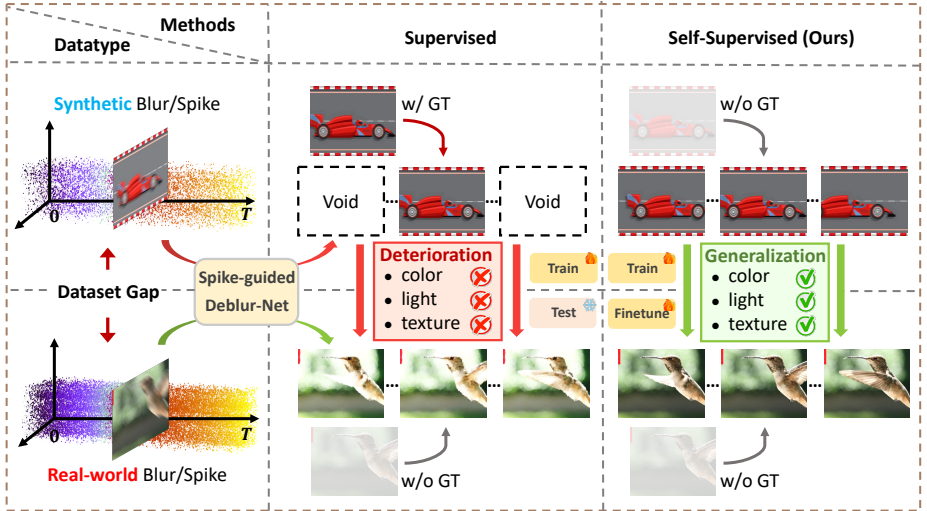


Fig. 1: Illustration of the superiority of our self-supervised framework (S-SDM) over supervised methods, where “” symbolizes active network training and “” indicates that network parameters remain unchanged during this stage. Supervised methods, while effective on synthetic datasets, suffer from a significant performance decline when applied to real-world datasets, primarily due to data distribution discrepancies. In contrast, our self-supervised framework, necessitating no Ground Truth (GT) for training, seamlessly bridges this dataset gap through fine-tuning on real-world datasets.

1 Introduction

Traditional cameras, constrained by their exposure-based imaging mechanism, often produce blurry images when capturing fast-moving objects or during camera movement throughout the exposure process [19, 28]. While these blurry images lose significant details, the ability to recover dynamic motion trajectories from the static blurry input becomes critically important. However, the inherent challenge lies in the limited motion features available within blurry frames, leading to potential ambiguities such as multiple motion trajectories corresponding to the same blurry input. This is exemplified by scenarios where two objects move along the same trajectory but in opposite directions [22, 23, 25, 30, 31], rendering the task of motion deblurring ill-posed. Recent advancements in learning-based approaches [12, 32, 38] seek to address this challenge by establishing direct mappings from blurry inputs to sharp sequences in a self-supervised manner. Despite these efforts, traditional cameras struggle to capture fine details in high-speed motion due to their exposure constraints, thus limiting the effectiveness of these methods in scenarios not covered by the training datasets.

In recent years, neuromorphic cameras [9, 10], leveraging their ultra-high temporal resolution and high dynamic range, have found widespread use in many fields, including computational imaging, computer vision, and robotics. These

cameras, including event and spike cameras, are distinguished by their ability to produce high temporal resolution outputs directly tied to changes in light intensity. Specifically, event cameras generate events in areas where light intensity changes [4], while spike cameras capture the absolute brightness of the scene at each pixel, offering a stream of spikes as output [10]. This distinctive feature endows spike cameras with a significant advantage in capturing and recovering texture information from scenes with rapid motion as validated by numerous recent studies [5, 6, 33, 37, 39, 40].

Recent studies [2, 8] have explored the potential of RGB-Spike fusion, *i.e.*, harnessing the strengths of both traditional and spike cameras to reconstruct sharp sequences from blurry inputs. However, their frameworks are constrained within the supervised learning paradigm, which necessitates extensive datasets comprising pairs of blurry and sharp images, as well as spike sequences. While synthetically acquiring such paired data, as demonstrated in previous studies [4, 8, 23], is feasible, collecting them in real-world scenarios presents several challenges: (1) high-speed cameras are prohibitively expensive and not readily deployable in many settings; (2) spatial-temporal calibration between spike cameras and high-speed RGB cameras complicates the data collection process. These challenges render the fine-tuning of supervised methods on real-world datasets impossible, further leading to their performance deterioration in such environments as shown in Fig. 1. The resulting degradation in image quality, manifesting as color distortion, brightness inconsistency, and inaccurate texture restoration, is mainly caused by the disparity between synthetic and real-world datasets, especially in terms of the density of spike stream, spike generation mechanism, and blurry image generation. Moreover, the effectiveness of supervised methods is inherently limited by the ground truth sequences created through motion analysis interpolation algorithms [11, 21], which inherently differs from the real-world scene and thus affects the model’s generalization ability.

To overcome these issues, we propose the first-of-its-kind **Self-supervised Spike-guided Deblurring Model (S-SDM)**, capable of recovering the continuous sharp sequence from a single blurry input with the assistance of low-resolution spike streams. We begin with a theoretical analysis of the relationship between spike streams, blurry images, and sharp sequences, leading to the development of our Spike-guided Deblurring Model (SDM). We further construct a self-supervised processing pipeline by cascading the denoising network and the super-resolution network to reduce the sensitivity of the SDM to spike noise and its reliance on spatial-resolution matching between the two modalities. To reduce the time consumption and enhance the utilization of spatial-temporal spike information within this pipeline, we further design a **Lightweight Deblurring Network (LDN)** and train it based on pseudo-labels from the teacher model, *i.e.*, the established self-supervised processing pipeline. By further introducing re-blurring loss during LDN training, we achieve better restoration performance and faster processing speed compared to the processing-lengthy and structure-complicated teacher model. To validate the performance of our S-SDM across various scenarios, we build an RGB-Spike binocular system and propose the first

spatially-temporally calibrated real-world spike blur dataset in this community. Quantitative and qualitative experiments conducted on our real-world and synthetic datasets with spikes validate the superior generalization of our S-SDM.

In summary, the key contributions of this paper are:

- We develop a self-supervised spike-guided image deblurring framework, addressing the performance degradation due to the synthetic-real domain gap that existed in previous supervised methods.
- We perform an in-depth theoretical analysis of the fusion between the spike stream and blurry image, leading to the development of the SDM.
- We propose a real-world blur dataset and experiments on real-world and synthetic datasets validate the superior generalization of our S-SDM.

2 Related Work

Spike Camera. The spike camera, inspired by the primate retina, stands apart from conventional cameras with its ability to generate synchronous spike streams for each pixel at extremely low latency. This distinct feature provides significant advantages in various applications such as high-speed imaging [5, 6, 33, 37, 39, 40], optical flow estimation [35], object detection [36], depth estimation [27], motion deblurring [8], and occlusion removal [26].

Spike-guided Motion Deblurring. While the spike camera boasts an ultra-high temporal resolution, its development is currently impeded by the low spatial resolution. Additionally, the single-channel output from the spike camera restricts previous methods from recovering the image color information. To address these issues, a promising approach is establishing an RGB-Spike hybrid imaging system [2]. The binocular system achieves the multi-modality fusion of High-spatial/Low-temporal RGB blurry input and High-temporal/Low-spatial spike stream, thereby also serving as a spike-guided motion deblurring method [8]. However, to the best of our knowledge, existing spike-guided deblurring methods [2, 8] predominantly rely on supervised training on synthetic datasets. This reliance results in significant performance degradation when these methods are evaluated in real-world scenarios due to the domain discrepancies between synthetic and real datasets as illustrated in Fig. 1.

Event-based Motion Deblurring. Event camera [20] can asynchronously generate events that record log-intensity changes at the pixel level with minimal latency, which contains a rich set of motion features beneficial for motion deblurring tasks. Numerous supervised methods [3, 4, 16, 16, 22, 23] have been proposed to learn the mapping from the blurry input, events to the sharp outcome. Despite these advancements, a major hurdle remains in obtaining real blurry-sharp image pairs for training. To overcome the domain gap between synthetic and real-world datasets, recent methods [25, 30, 31] explored the mutual constraint between the blurry image and event stream, enabling the training of networks on real-world blur datasets.

3 Method

3.1 Preliminaries

Spike Camera Mechanism. Consider $\mathbf{L}(t)$ to represent the latent sharp frame at time t . Each pixel p in the spike camera [10] has an integrator that accumulates the incoming photons at a high frequency. Once the cumulative intensity exceeds a predefined threshold C at time t_e , pixel p emits a spike, and the accumulation of photons is reset to zero. This process can be mathematically described as follows:

$$\int_{t_s}^{t_e} \mathbf{L}(t) dt \geq C, \quad (1)$$

where t_s denotes the firing time of the previous spike. While the spike camera is capable of generating asynchronous spike streams akin to that of event cameras, its effectiveness is constrained by the inherent limitations of its physical circuitry, which necessitates reading spikes at a predetermined sampling rate. We denote the generated spike stream as $\mathcal{S} \in \{0, 1\}^{K \times H \times W}$, where H and W signify the height and width of the image, and K represents the length of the spike sequence.

Problem Formulation. In traditional photography, motion blur occurs when there is relative movement between the camera and the scene during the exposure period. According to the motion blur physical model [9], the blurry image \mathbf{B} can be represented as the average of the latent frame $\mathbf{L}(t)$ over the exposure \mathcal{T} , *i.e.*:

$$\mathbf{B} = \frac{1}{T} \int_{t \in \mathcal{T}} \mathbf{L}(t) dt, \quad (2)$$

where T represents the exposure period. Despite the spike camera’s superior temporal resolution, its spatial resolution remains comparatively low. This limitation is primarily attributed to the constraints in data transmission bandwidth and the challenges inherent in the manufacturing process. Here, we postulate that the spatial resolution of the spike camera is approximately one-quarter that of a conventional RGB camera.

In this paper, we aim to enhance the High-spatial/Low-temporal resolution blurry input $\mathbf{B} \in \mathbb{R}^{1 \times 3 \times H \times W}$ into a sequence of High-Quality images $\{\mathbf{L}(t_i)\}_{i=1}^K \in \mathbb{R}^{K \times 3 \times H \times W}$ with the aiding of High-temporal/Low-spatial resolution spike stream $\mathcal{S}_{\mathcal{T}} \in \{0, 1\}^{K \times 1 \times \frac{H}{4} \times \frac{W}{4}}$, which can be mathematically formulated as:

$$\{\mathbf{L}(t_i)\}_{i=1}^K = \text{Deblur}(t_i; \mathbf{B}, \mathcal{S}_{\mathcal{T}}). \quad (3)$$

In Eq. (3), $\text{Deblur}(\cdot)$ represents the Spike-guided Deblur-Net as shown in Fig. 1, i refers to the i -th frame in the spike stream $\mathcal{S}_{\mathcal{T}}$, and t_i is the timestamp associated with this frame.

3.2 Theoretical Analysis

The spike camera, with its photodetector tailored to capture the single-channel light intensity, faces difficulties in obtaining the color information that the multi-channel RGB camera can effortlessly capture. Therefore, we modify the color

intensity $\mathbf{L}(t)$ in Eq. (1) to the grayscale value $\mathbf{L}_g(t)$ for further analysis:

$$\int_{t_s}^{t_e} \mathbf{L}_g(t) dt \geq C. \quad (4)$$

In this formulation, $\mathbf{L}_g(t) = w_r \cdot \mathbf{L}_r(t) + w_{gre} \cdot \mathbf{L}_{gre}(t) + w_b \cdot \mathbf{L}_b(t)$, where $\mathbf{L}_c(t)$, w_c denote the intensity and weight of channel $c \in \{r, gre, b\}$ respectively.

Given the blurry input \mathbf{B} and its corresponding spike stream $\mathcal{S}_{\mathcal{T}}$, we incorporate Eq. (4) into the motion blur model presented in Eq. (2). This integration formulates a link between the two modalities as outlined below:

$$\mathbf{B}_g = \frac{C \cdot N_{\mathcal{T}}}{T}, \quad (5)$$

where \mathbf{B}_g denotes the grayscale version of the blurry input, and $N_{\mathcal{T}}$ denotes the total number of spikes accumulated over the exposure period, as shown in Fig. 2(a). The accumulation $N_{\mathcal{T}}$ is calculated as $N_{\mathcal{T}} = \sum_{i=1}^K \mathcal{S}[i]$, with $\mathcal{S}[i]$ indicating the i -th frame of the spike stream.

Within the exposure \mathcal{T} , we consider a shorter spike sequence centered around the t moment $\mathcal{S}_{\mathcal{T}'} \in \{0, 1\}^{K' \times 1 \times H \times W}$, satisfying $K' \ll K$, $t \in \mathcal{T}$, and $\mathcal{T}' \subset \mathcal{T}$. Similar to Eq. (5), we can derive the relationship between the short-exposure gray image $B_g(t, \mathcal{T}')$ and the short spike stream $\mathcal{S}_{\mathcal{T}'}$ as follows:

$$B_g(t, \mathcal{T}') = \frac{1}{T'} \int_{s \in \mathcal{T}'} \mathbf{L}(s) ds = \frac{C \cdot N_{\mathcal{T}'}}{T'}, \quad (6)$$

where $T' \ll T$ represents the short exposure time. We adopt a notation in which the bolded symbol \mathbf{B}_g signifies the image captured by conventional cameras, whereas the non-bolded expression $B_g(t, \mathcal{T}')$ corresponds to images reconstructed from the spike stream, as depicted in Fig. 2(a).

Given the observation that the color information of adjacent pixels often exhibits similarity under the premise of minor motion amplitude, we postulate that the colors of the blurry input \mathbf{B} and the short-exposure image $B(t, \mathcal{T}')$ are identical. This assumption implies that the intensity proportion among RGB channels in two images $\alpha_c / \alpha_c(t, \mathcal{T}')$ is approximately equivalent, *i.e.*, $\alpha_c \approx \alpha_c(t, \mathcal{T}')$, satisfying $\alpha_c = \mathbf{B}_g / \mathbf{B}_c$ and $\alpha_c(t, \mathcal{T}') = B_g(t, \mathcal{T}') / B_c(t, \mathcal{T}')$. More details can be found in the supplementary materials.

Upon establishing it, we move forward to build a mathematical relation between the two images. By substituting the gray channel g with color channel c and dividing Eq. (5) by Eq. (6), we efficiently eliminate the unknown threshold C and weights, leading to the following equation:

$$B_c(t, \mathcal{T}') = \mathbf{B}_c \cdot \frac{N_{\mathcal{T}'}}{N_{\mathcal{T}}} \cdot \frac{T}{T'}. \quad (7)$$

By applying Eq. (7) to RGB three channels, we explicitly establish the relationship between the color blurry input \mathbf{B} , the color short-exposure image $B(t, \mathcal{T}')$ and the spike stream $\mathcal{S}_{\mathcal{T}}$ as shown in Fig. 2(a). Since the exposure

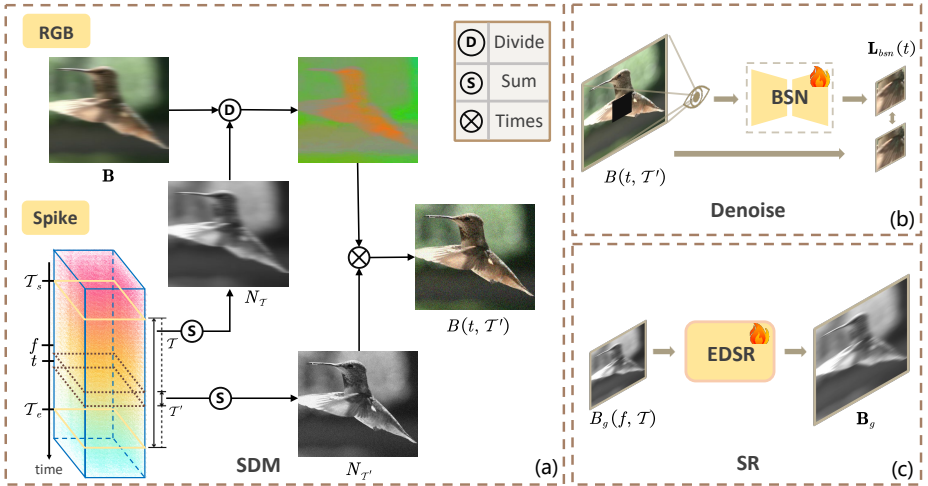


Fig. 2: The schematic diagram presents the SDM model (a), the denoising network (b), and the SR network (c). In these diagrams, “” symbolizes the network is trained during this stage. Additionally, the black hole in (b) signifies that the information in this area is not accessible to the BSN.

period \mathcal{T}' is relatively short, it is reasonable to assume that the scene remains static. In this context, we interpret the short-exposure image $B(t, \mathcal{T}')$ as the latent sharp frame $L(t)$, allowing us to modify Eq. (7) as follows:

$$\mathbf{L}(t) = \mathbf{B} \cdot \frac{N_{\mathcal{T}'}}{N_{\mathcal{T}}} \cdot \frac{T}{T'}. \quad (8)$$

To this end, we have conducted a comprehensive theoretical analysis of the spike-guided motion deblurring task, which is neglected in prior learning-based motion deblurr methodologies [2, 8]. For further discussion readability, we refer to Eq. (8) as the **Spike-guided Deblurring Model (SDM)** as shown in Fig. 2(a), which is analogous to the baseline motion deblurr model EDI [18] in event camera.

3.3 Self-supervised Spike-guided Deblurring Model

While SDM theoretically allows for the fusion of the blurry image and the spike stream, its practical deployment faces the following obstacles:

- The deblurred image $B(t, \mathcal{T}')$ suffers from noise-related degradation attributed to the lack of adequate spike information during the short exposure \mathcal{T}' .
- The spatial resolution of the spike camera is approximately one-quarter of the RGB camera, rendering the SDM implementation impractical.

To tackle these limitations, we first devise a lengthy yet feasible processing pipeline based on the SDM, as illustrated in the Fig. 3. Initially, we utilize

Eq. (6) to convert the short-exposure spike stream into an image, followed by a sequential cascade of the Denoising Network and the Super-Resolution Network, which are tasked with denoising and resolution-enhancement respectively in a self-supervised manner. Subsequently, the deblurred image is obtained through the SDM, with inputs comprising both the blurry image and the enhanced short-exposure image. In the following, we delve into the details of the Denoising Network and Super-Resolution Network.

Denoising Network. To this end, We leverage the powerful self-supervised denoising capabilities of the Blind Spot Network (BSN) [1, 5, 7, 13, 14, 24]. The core idea of BSN involves designing the blind-spot mechanism, which compels the network to estimate the value of each pixel based on the intensities of its surrounding pixels, as illustrated in Fig. 2(b). Under the premise that the noise is random and independent, the BSN can be trained to accurately predict the value of clean pixels and deduce the appropriate values for noisy pixels from their surroundings.

In the pre-training part of our processing pipeline, the short-exposure noisy image $B(t, \mathcal{T}')$ serves as both the input and the supervision signal for the BSN [13] with the loss function formulated as:

$$\mathcal{L}_{BSN} = \|B(t, \mathcal{T}') - \text{BSN}(B(t, \mathcal{T}'); \Theta_1)\|_2^2, \quad (9)$$

where Θ_1 represents the parameters of the BSN. Once the BSN is trained, we feed the noisy image into it to yield the denoised image $\mathbf{L}_{bsn}(t)$.

Super-Resolution Network. In this task, we observe that the blurry input \mathbf{B} from the RGB camera and the long-exposure image $B(f, \mathcal{T})$ from the spike camera, where f is the central moment during the exposure shown in Fig. 2(a), exhibit similar characteristics. This motivates us to train the SR network based on these pairs as shown in Fig. 2(c) and subsequently apply it to enhance the resolution of the short-exposure image.

We leverage the well-explored network Enhanced Deep Super-Resolution network (EDSR) [15] as the backbone of our SR network, with the long-exposure image $B_g(f, \mathcal{T}) \in \mathbb{R}^{1 \times \frac{H}{4} \times \frac{W}{4}}$ as the input and the blurry gray input $\mathbf{B}_g \in \mathbb{R}^{1 \times H \times W}$ as supervision. The loss function is formulated as follows:

$$\mathcal{L}_{SR} = \|\mathbf{B}_g - \text{EDSR}(B_g(f, \mathcal{T}); \Theta_2)\|_2^2, \quad (10)$$

where Θ_2 represents the parameters of the EDSR. Subsequently, we freeze the network parameters and apply it to the denoised short-exposure image $\mathbf{L}_{bsn}(t)$, yielding the resolution-enhanced image $\mathbf{L}_{bsn}^\uparrow(t)$.

Lightweight Deblur Network. While the aforementioned processing pipeline successfully achieves the multi-modality fusion of the High-spatial/Low-temporal blurry input and the High-temporal/Low-spatial spike stream, several aspects still need refinement:

- The framework is lengthy and computationally demanding, which hinders its suitability for real-time system deployment.

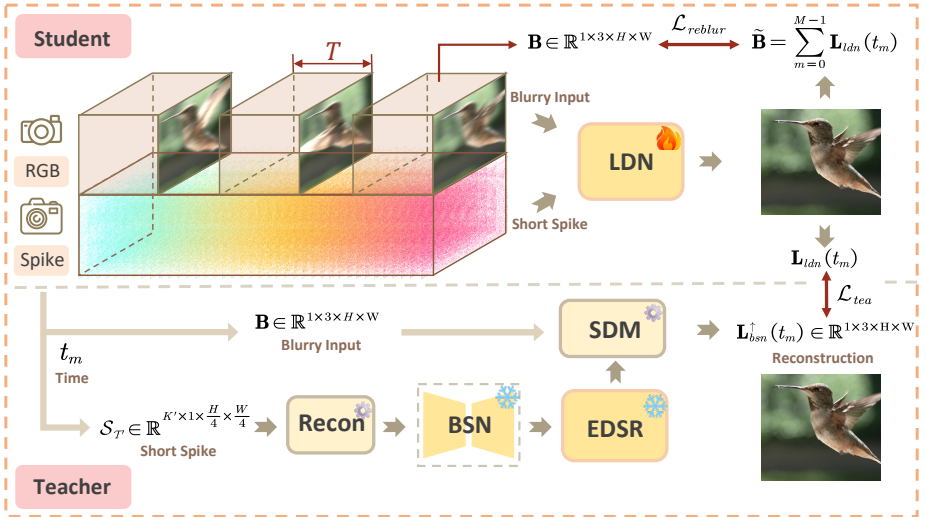


Fig. 3: The schematic diagram of our proposed distillation self-supervised framework, where “Recon” denotes the short-exposure image reconstruction corresponding to Eq. (6). In this diagram, the “❄️” symbol denotes that the network parameters are frozen during this stage, while the “⚙️” indicates that certain computations are executed in a non-network manner.

- The blind-spot strategy of the BSN limits the full utilization of the spatial information inherent in the spike stream.
- The representation of the short-exposure image does not fully reflect the advantages of the high temporal resolution inherent in the spike stream.

To improve them, we further build a knowledge distillation framework building upon the existing processing pipeline, which provides the reconstructed sequence as pseudo-labels for the training of the student network LDN as shown in Fig. 3. LDN adheres to a similar input and output pattern as [8], *i.e.*, taking the blurry input \mathbf{B} and the short spike stream $\mathcal{S}_{\mathcal{T}}$ centered around moment t as inputs, with the output being the reconstructed sharp image $\mathbf{L}_{ldn}(t)$. The mapping relationship of the LDN can be mathematically formulated as follows:

$$\mathbf{L}_{ldn}(t) = \text{LDN}(\mathbf{B}, \mathcal{S}_{\mathcal{T}}; \Theta_3), \quad (11)$$

where Θ_3 represents the parameters of the LDN. The LDN is designed according to the encoder-fusion-decoder paradigm [4, 8, 23]. Full details regarding its structure are available in the supplementary materials.

In real-world scenarios where ground truth images are unavailable for supervision, we employ the previously described processing pipeline as the teacher model. To avoid the scenario where the LDN exactly replicates the mapping of the teacher model, we construct the teacher loss \mathcal{L}_{tea} based on the LPIPS [29] and further introduce the blur reconstruction loss. The reblur loss \mathcal{L}_{reblur} measures the difference between the blurry input \mathbf{B} and the re-synthesized blurry

image $\tilde{\mathbf{B}}$, satisfying:

$$\tilde{\mathbf{B}} = \sum_{m=0}^{M-1} \mathbf{L}_{ldn}(t_m), \quad (12)$$

where $\mathbf{L}_{ldn}(t_m)$ represents the m -th recovered image within the exposure period \mathcal{T} and M is the total number of reconstructed images. To sum up, the final loss function for our knowledge distillation framework is formulated as follows:

$$\mathcal{L} = \mathcal{L}_{tea} + \lambda \cdot \mathcal{L}_{reblur} \quad (13)$$

$$= \sum_{m=0}^{M-1} \mathcal{L}_{LPIPS}(\mathbf{L}_{bsn}^{\uparrow}(t_m), \mathbf{L}_{ldn}(t_m)) + \lambda \cdot \mathcal{L}_{MSE}(\tilde{\mathbf{B}}, \mathbf{B}), \quad (14)$$

where $\mathbf{L}_{bsn}^{\uparrow}(t_m)$ represents the denoising result after being upscled by the SR network, and λ is a weighting parameter.

4 Experiments

4.1 Dataset

Synthetic Data. For quantitative and qualitative analysis of our spike-guided motion deblurring task, we construct the synthetic dataset based on the widely employed motion deblur dataset GOPRO [17] with the resolution of 1280×720 . Initially, we utilize the interpolation algorithm XVFI [21] to augment the video frame by interpolating additional 7 frames between each pair of consecutive sharp images. To generate the spike stream that mimics reality closely, we downsample the interpolated video to the resolution of 320×180 and simulate the spike stream based on the spike simulator [34] modeled according to the spike generation physical model. To replicate real-world motion blur, we synthesize each blurry input by averaging 97 frames from interpolated video sequences.

Real-world Data. To comprehensively assess the deblurring performance of our S-SDM in real-world scenarios, we construct an RGB-Spike binocular system and propose the first **Real-world Spike-guided Blur (RSB)** dataset in this community. This system consists of a fixed-exposure RGB camera (Basler acA1920-150uc) and a spike camera [10], enabling us to capture the blurry image and the corresponding spike stream simultaneously. Further details about our RSB and the spatial-temporal calibration for our binocular system are provided in the supplementary materials.

4.2 Experimental Results

We conduct both quantitative and qualitative comparisons of our S-SDM against state-of-the-art (SOTA) methods, including frame-based Motion-ETR [32], LEVS [12], video-based BiT [38] and spike-based SpkDeblurNet [8] on the GOPRO and RSB datasets. Since SpkDeblurNet does not fully consider the real spatial-resolution gap between two modalities in real-world scenarios, we modify its spike

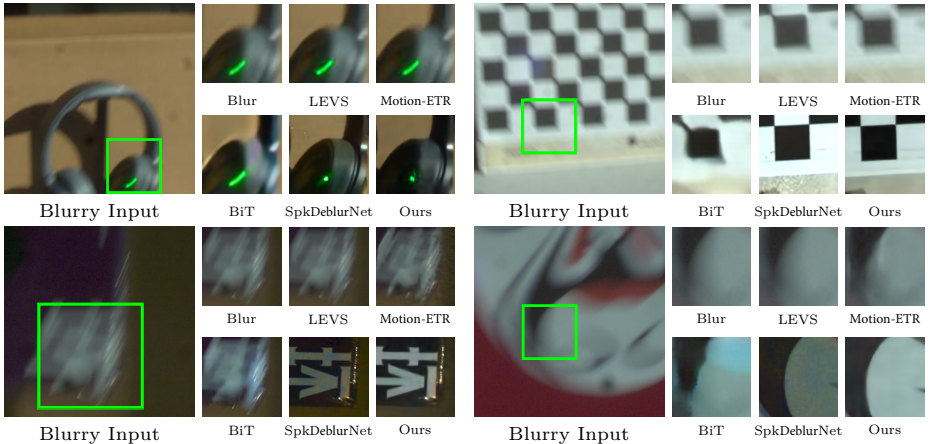


Fig. 4: Qualitative comparison for the single frame restoration on the RSB dataset.

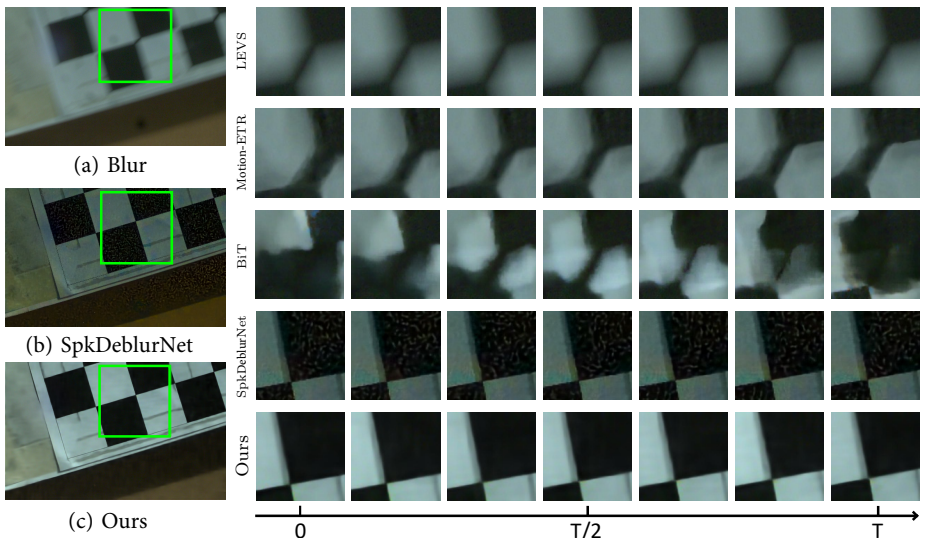


Fig. 5: Qualitative comparison for the sequence reconstruction on the RSB dataset.

down-sampling module to perform convolution at the original size and retrain it on our synthetic dataset for a fair comparison.

GOPRO Dataset. We reconstruct 7 images from one blurry input for sequence restoration evaluation [31] as detailed in Tab. 1. Given that the principal contribution of the S-SDM is self-supervised learning, it is foreseeable that our method might be slightly inferior to the supervised method SpkDeblurNet on the GOPRO synthetic dataset. Revisiting the mentioned motion ambiguity problem, we observe that frame-based methods LEVS and Motion-ETR suffer significant performance degradation in transitioning from single frame restoration to sequence reconstruction, with decreases of 4.425 dB \downarrow and 5.866 dB \downarrow in PSNR

Table 1: Quantitative comparison of the single frame and sequence reconstruction task on the GOPRO dataset, where ‘GT’ indicates that this method requires ground truth for training and ‘Single Frame’ refers to the middle frame of the restored sequence.

Methods	Inputs		GT	Single Frame		Sequence		Params
	RGB	Spike		PSNR \uparrow	SSIM \uparrow	PSNR \uparrow	SSIM \uparrow	
LEVS [12]	✓	×	✓	25.400	0.727	21.155	0.601	<u>4.97M</u>
Motion-ETR [32]	✓	×	✓	27.821	0.763	21.955	0.610	6.55M
BiT [38]	✓	×	✓	24.442	0.724	23.644	0.698	11.3M
SpkDeblurNet [8]	✓	✓	✓	32.108	0.873	30.712	0.821	13.4M
S-SDM (Ours)	✓	✓	×	<u>27.928</u>	<u>0.786</u>	<u>26.893</u>	<u>0.757</u>	0.234M

respectively. In contrast, our method alleviates this issue benefiting from the incorporation of the high temporal-resolution spike stream.

RSB Dataset. We further present visualizations of single frame and sequence reconstruction comparisons on the real-world RSB dataset. For the single frame restoration qualitative experiments as depicted in Fig. 4, both frame-based and video-based approaches fail to replicate fine textures and detailed elements present in the blurry input. While SpkDeblurNet is capable of recovering structural details, it is deteriorated by significant noise and color distortion under conditions with lower spike density than those simulated in the GOPRO dataset. Similarly, in scenarios of higher spike stream densities, the restoration of SpkDeblurNet tends to exhibit over-exposure, resulting in brightness inconsistency compared to the blurry input. In terms of high-frequency details, other methods struggle to eliminate the laser ghost as evident in the earphone scene of Fig. 4.

In the qualitative experiments focusing on sequence restoration as in Fig. 5, LEVS fails to analyze motion information during the exposure, resulting in uniform outcomes across each image in the sequence. While Motion-ETR and BiT appear to trace the moving pattern of the calibration board correctly, the texture restoration is severely destroyed. Benefiting from the incorporation of the spike stream, though SpkDeblurNet correctly recovers the trajectory, it encounters deterioration problems similar to those observed in Fig. 5. Our method tackles the aforementioned challenges in a self-supervised manner, which facilitates re-training on the real-blur dataset, ensuring that the restored sequence is aligned with the real-captured blurry input and spike stream. More comparative experiments and analyses are accessible in the supplementary material.

4.3 Ablation Study

In this subsection, we perform ablation experiments on the GOPRO and RSB datasets to evaluate the performance of each module within S-SDM, as well as the overall effectiveness of our distillation learning framework.

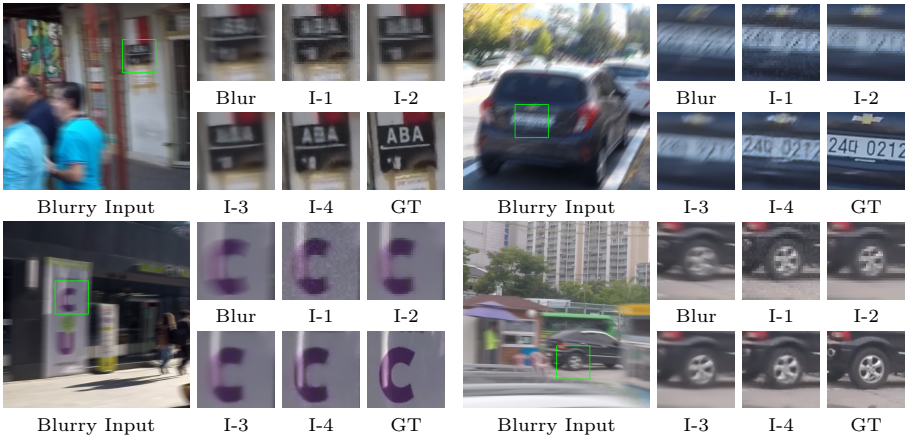
Modules Cascading. Building upon the SDM, we sequentially cascade the denoising network, the SR network, and the LDN to evaluate their respective

Table 2: Ablation study for evaluating the modules of S-SDM.

ID	BSN	SR	LDN	PSNR \uparrow	SSIM \uparrow
I-1	×			22.943	0.461
I-2	✓			24.490	0.645
I-3	✓	✓		26.144	0.708
I-4	✓	✓	✓	27.928	0.786

Table 3: Ablation study for evaluating the effectiveness of the distillation framework.

ID	\mathcal{L}_{tea}	\mathcal{L}_{reblur}	λ	PSNR \uparrow	SSIM \uparrow
II-1	×	✓	10	23.102	0.441
II-2	✓	×	/	26.713	0.723
II-3	✓	✓	10	27.380	0.762
II-4	✓	✓	50	27.804	0.779
II-5	✓	✓	70	27.825	0.780
II-6	✓	✓	100	27.928	0.786

**Fig. 6:** Ablation study for evaluating modules of S-SDM on the GOPRO dataset. Experiments corresponding to the ID can be viewed through Tab. 2.

effectiveness. The quantitative ablation experiments are presented in Tab. 2. Given that the spatial resolution of the spike camera is one-quarter of that of conventional cameras, we employ nearest neighbor interpolation as a substitute for the SR network in experiments I-1 and I-2 to align the spatial resolution of two modalities.

Qualitative comparisons based on the GOPRO dataset are illustrated in Fig. 6. These comparisons reveal that although the SDM is effective in removing motion blur, it struggles with significant noise and detail loss, attributed to the inherent spike noise and the relatively low spatial resolution of the spike camera. While the BSN mitigates noise and the SR network improves image resolution explicitly, the LDN trained via distillation learning further refines these enhancements, enabling the recognition of intricate textural features in the images, such as the license plate and the door number shown in Fig. 6.

Distillation Learning. In this part, we concentrate on analyzing the contribution of reblur loss \mathcal{L}_{reblur} and teacher loss \mathcal{L}_{tea} within the distillation framework. Diverging from the reconstruction loss designed in EVDI [30], which utilizes two adjacent blurry images for mutual constraint, our reblur loss relies solely on a single blurry frame. Therefore, it becomes evident that the LDN

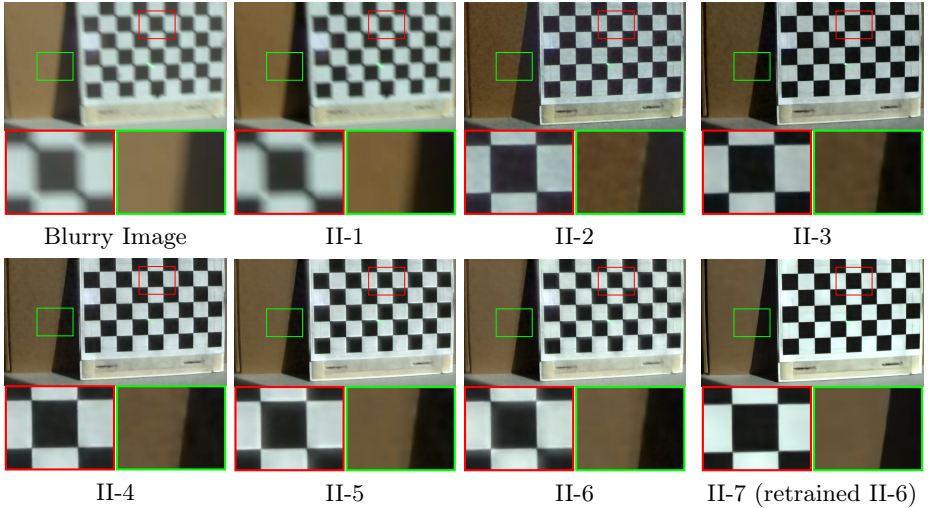


Fig. 7: Ablation study for evaluating the overall effectiveness of our distillation learning framework on the RSB dataset. The details corresponding to the experiment ID can be viewed through the Tab. 3.

tends toward learning identity mapping from the blurry input in the absence of supervision from the teacher network. Nevertheless, under the guidance of the teacher model, the reblur loss \mathcal{L}_{reblur} plays a dual role. It not only enforces motion consistency in the reconstructed sequence but also enriches the LDN with high-resolution details from the non-blurry regions of the blurry input. Quantitative evaluations conducted on the GOPRO synthetic dataset, as detailed in Tab. 3, demonstrate that the incorporation of reconstruction loss enhances the performance of LDN. Notably, within a specific range, an increase in the hyperparameter λ correlates with improved performance.

We directly apply the LDN initially trained on the GOPRO synthetic dataset to real-world scenarios, with qualitative visualization illustrated in Fig. 7. As observed in the results, the absence of the reblur loss \mathcal{L}_{reblur} leads to significant noise in the background of the recovered image, which predominantly arises from the disparity in spike stream density between the simulated and real-captured stream. This discrepancy causes the LDN to overestimate the spike count, resulting in ‘black holes’ in regions with lower spike density as depicted in the brown board of Fig. 7, which reflects the drawback inherent in the supervised learning strategies as discussed in Sec. 1. Increasing the weight of the reblur loss \mathcal{L}_{reblur} allows the LDN to incorporate more information from the blurry input, thereby mitigating this issue. However, this adjustment also leads to the presence of blurry edges. We further retrain the LDN on the RSB dataset (referred to as Experiment II-7), following the parameters set in Experiment II-6. The retrained LDN effectively recovers the sharp edge of the calibration board and suppresses the spike noise in the background, validating the feasibility of our self-supervised framework in real-world scenarios.

5 Conclusion

In this paper, we have looked into a novel self-supervised framework S-SDM for spike-guided motion deblurring, which reconstructs sequences of sharp images from real-world blurry inputs alongside the corresponding spike stream. We initially propose the physical model SDM for this task and subsequently construct a self-supervised processing pipeline to overcome the challenges of spike noise and spatial resolution mismatch inherent in the SDM. We further design the distillation-based LDN to enhance the restoration performance. In addition, we construct an RGB-Spike binocular system and propose the first spatially-temporally calibrated real-world dataset RSB in this community. Quantitative and qualitative experiments conducted on our real-world and synthetic datasets with spikes validate the superior generalization of our proposed S-SDM.

References

1. Byun, J., Cha, S., Moon, T.: Fbi-denoiser: Fast blind image denoiser for poisson-gaussian noise. In: CVPR. pp. 5768–5777 (2021)
2. Chang, Y., Zhou, C., Hong, Y., Hu, L., Xu, C., Huang, T., Shi, B.: 1000 fps hdr video with a spike-rgb hybrid camera. In: CVPR. pp. 22180–22190 (2023)
3. Chen, H., Teng, M., Shi, B., Wang, Y., Huang, T.: A residual learning approach to deblur and generate high frame rate video with an event camera. IEEE TMM (2022)
4. Chen, K., Yu, L.: Motion deblur by learning residual from events. IEEE TMM (2024)
5. Chen, S., Duan, C., Yu, Z., Xiong, R., Huang, T.: Self-supervised mutual learning for dynamic scene reconstruction of spiking camera. In: IJCAI. pp. 2859–2866 (2022)
6. Chen, S., Yu, Z., Huang, T.: Self-supervised joint dynamic scene reconstruction and optical flow estimation for spiking camera. In: AAAI. pp. 350–358 (2023)
7. Chen, S., Zhang, J., Yu, Z., Huang, T.: Exploring asymmetric tunable blind-spots for self-supervised denoising in real-world scenarios. arXiv preprint arXiv:2303.16783 (2023)
8. Chen, S., Zhang, J., Zheng, Y., Huang, T., Yu, Z.: Enhancing motion deblurring in high-speed scenes with spike streams. In: NeurIPS (2023)
9. Gallego, G., Delbrück, T., Orchard, G., Bartolozzi, C., Taba, B., Censi, A., Leutenegger, S., Davison, A.J., Conradt, J., Daniilidis, K., et al.: Event-based vision: A survey. IEEE TPAMI **44**(1), 154–180 (2020)
10. Huang, T., Zheng, Y., Yu, Z., Chen, R., Li, Y., Xiong, R., Ma, L., Zhao, J., Dong, S., Zhu, L., et al.: 1000× faster camera and machine vision with ordinary devices. Engineering **25**, 110–119 (2023)
11. Huang, Z., Zhang, T., Heng, W., Shi, B., Zhou, S.: Real-time intermediate flow estimation for video frame interpolation. In: ECCV. pp. 624–642. Springer (2022)
12. Jin, M., Meishvili, G., Favaro, P.: Learning to extract a video sequence from a single motion-blurred image. In: CVPR. pp. 6334–6342 (2018)
13. Laine, S., Karras, T., Lehtinen, J., Aila, T.: High-quality self-supervised deep image denoising. NeurIPS **32** (2019)
14. Lee, W., Son, S., Lee, K.M.: Ap-bsn: Self-supervised denoising for real-world images via asymmetric pd and blind-spot network. In: CVPR. pp. 17725–17734 (2022)
15. Lim, B., Son, S., Kim, H., Nah, S., Mu Lee, K.: Enhanced deep residual networks for single image super-resolution. In: CVPR. pp. 136–144 (2017)
16. Lin, S., Zhang, J., Pan, J., Jiang, Z., Zou, D., Wang, Y., Chen, J., Ren, J.: Learning event-driven video deblurring and interpolation. In: ECCV. pp. 695–710. Springer (2020)
17. Nah, S., Kim, T.H., Lee, K.M.: Deep multi-scale convolutional neural network for dynamic scene deblurring. In: CVPR (July 2017)
18. Pan, L., Scheerlinck, C., Yu, X., Hartley, R., Liu, M., Dai, Y.: Bringing a blurry frame alive at high frame-rate with an event camera. In: CVPR. pp. 6820–6829 (2019)
19. Peterson, B.: Understanding exposure: how to shoot great photographs with any camera. AmPhoto books (2016)
20. Serrano-Gotarredona, T., Linares-Barranco, B.: A 128×128 1.5% contrast sensitivity 0.9% fpn 3 μ s latency 4 mw asynchronous frame-free dynamic vision sensor using transimpedance preamplifiers. IEEE Journal of Solid-State Circuits **48**(3), 827–838 (2013)

21. Sim, H., Oh, J., Kim, M.: Xvfi: extreme video frame interpolation. In: ICCV. pp. 14489–14498 (2021)
22. Song, C., Huang, Q., Bajaj, C.: E-cir: Event-enhanced continuous intensity recovery. In: CVPR. pp. 7803–7812 (2022)
23. Sun, L., Sakaridis, C., Liang, J., Jiang, Q., Yang, K., Sun, P., Ye, Y., Wang, K., Gool, L.V.: Event-based fusion for motion deblurring with cross-modal attention. In: ECCV. pp. 412–428. Springer (2022)
24. Wang, Z., Liu, J., Li, G., Han, H.: Blind2unblind: Self-supervised image denoising with visible blind spots. In: CVPR. pp. 2027–2036 (2022)
25. Xu, F., Yu, L., Wang, B., Yang, W., Xia, G.S., Jia, X., Qiao, Z., Liu, J.: Motion deblurring with real events. In: ICCV. pp. 2583–2592 (2021)
26. Zhang, J., Chen, S., Zheng, Y., Yu, Z., Huang, T.: Unveiling the potential of spike streams for foreground occlusion removal from densely continuous views. arXiv preprint arXiv:2307.00821 (2023)
27. Zhang, J., Tang, L., Yu, Z., Lu, J., Huang, T.: Spike transformer: Monocular depth estimation for spiking camera. In: ECCV. pp. 34–52. Springer (2022)
28. Zhang, K., Ren, W., Luo, W., Lai, W.S., Stenger, B., Yang, M.H., Li, H.: Deep image deblurring: A survey. *International Journal of Computer Vision* **130**(9), 2103–2130 (2022)
29. Zhang, R., Isola, P., Efros, A.A., Shechtman, E., Wang, O.: The unreasonable effectiveness of deep features as a perceptual metric. In: CVPR. pp. 586–595 (2018)
30. Zhang, X., Yu, L.: Unifying motion deblurring and frame interpolation with events. In: CVPR. pp. 17765–17774 (2022)
31. Zhang, X., Yu, L., Yang, W., Liu, J., Xia, G.S.: Generalizing event-based motion deblurring in real-world scenarios. In: ICCV. pp. 10734–10744 (2023)
32. Zhang, Y., Wang, C., Maybank, S.J., Tao, D.: Exposure trajectory recovery from motion blur. *PAMI* **44**(11), 7490–7504 (2021)
33. Zhao, J., Xiong, R., Liu, H., Zhang, J., Huang, T.: Spk2imgnet: Learning to reconstruct dynamic scene from continuous spike stream. In: CVPR. pp. 11996–12005 (2021)
34. Zhao, J., Zhang, S., Ma, L., Yu, Z., Huang, T.: Spikingsim: A bio-inspired spiking simulator. In: ISCAS. pp. 3003–3007. IEEE (2022)
35. Zhao, R., Xiong, R., Zhao, J., Yu, Z., Fan, X., Huang, T.: Learning optical flow from continuous spike streams. *NeurIPS* **35**, 7905–7920 (2022)
36. Zheng, Y., Yu, Z., Wang, S., Huang, T.: Spike-based motion estimation for object tracking through bio-inspired unsupervised learning. *IEEE TIP* **32**, 335–349 (2022)
37. Zheng, Y., Zheng, L., Yu, Z., Shi, B., Tian, Y., Huang, T.: High-speed image reconstruction through short-term plasticity for spiking cameras. In: CVPR. pp. 6358–6367 (2021)
38. Zhong, Z., Cao, M., Ji, X., Zheng, Y., Sato, I.: Blur interpolation transformer for real-world motion from blur. In: CVPR. pp. 5713–5723 (2023)
39. Zhu, L., Dong, S., Huang, T., Tian, Y.: A retina-inspired sampling method for visual texture reconstruction. In: ICME. pp. 1432–1437. IEEE (2019)
40. Zhu, L., Dong, S., Li, J., Huang, T., Tian, Y.: Retina-like visual image reconstruction via spiking neural model. In: CVPR. pp. 1438–1446 (2020)